J. Fluid Mech. (1988), *vol.* 196, *pp.* 39–63
Printed in Great Britain

Three-dimensional wave patterns generated by moving disturbances at transcritical speeds

By GEIR PEDERSEN
Department of Mechanics, University of Oslo, PO Box 1053, Blindern, 0316 Oslo 3, Norway

(Received 24 August 1987 and in revised form 18 February 1988)

Disturbances in the form of pressure fields, source distributions and time-dependent bottom topographies are discussed and found to produce similar wave patterns. Results obtained for wide channels are discussed in the light of the features of soliton reflection at a wall. Comparison with experiments shows excellent agreement. The introduction of radiation conditions enables long-time simulation of the development of wave patterns in infinite and semi-infinite fluids. A stationary wave pattern is also found to emerge for slightly supercritical Froude numbers, but contrary to linear results the leading divergent waves may originate ahead of the disturbance. This behaviour is due to nonlinear interactions similar to those governing collisions between solitons. This study on wave generation by a moving disturbance is based on numerical solutions of Boussinesq-type equations. The equations in their most general form are integrated by an implicit difference method. Strongly supercritical cases are described by a simplified set of equations which is solved by a semi-implicit difference scheme.

1. Introduction

According to linearized theory a steadily moving ship in an infinite fluid of constant depth always produces a stationary gravity-wave pattern in its wake. The qualitative properties of this pattern depend on the Froude number $F = U(gh_0)^{-\frac{1}{2}}$, which is the ratio of the speed of the ship and the maximum wave speed. In the limit $F \to 0$ we have the Kelvin ship-wave pattern for infinite depth where two types of wave crests, transverse and diverging, are confined to a sector of semiangle $\theta = 19.3°$. When F increases this angle increases and approaches 90° in the limit $F \to 1^-$. For $F > 1$ the transverse waves have disappeared and the angle of the wave sector again decreases, roughly according to $\theta = \arccos F^{-1}$.

In two dimensions linearized theory displays a singularity in the limit $F \to 1$ where the group velocity coincides with the speed of the ship and nonlinear effects have to be crucial. Laboratory studies on moving vessels in comparatively narrow channels have revealed that the physical response to this resonance is upstream radiation of solitons. The phenomenon was first reported by Thews & Landweber (1935). Later experimental investigations have been performed by Graff (1962), Schmidt-Stiebitz (1966), Huang *et al.* (1982). Ertekin (1984) and Ertekin, Webster & Wehausen (1984) identified the blockage coefficient as the important geometrical parameter. The blockage coefficient may be defined as the ratio of the cross-sections of the ship and the channel. Upstream radiation is also observed in comparatively wide channels. In such cases three-dimensional diverging waves develop into plane solitons propagating upstream relative to the ship.

The simplest theoretical approach to upstream soliton emission is perhaps to solve

equations of Boussinesq or KdV type with a moving pressure field applied to the free surface. Both Wu & Wu (1982) and Ertekin *et al.* (1984) found upstream radiation in the two-dimensional (horizontal and vertical) case. In a subsequent paper Ertekin, Webster & Wehausen (1986) reported some three-dimensional results obtained from the Green–Naghdi equation which is a Boussinesq-type equation with a nonlinear dispersion term. Upstream radiation was still predicted. It must however be noted that the calculations were confined to channels too narrow for three-dimensional effects to be very apparent during the generation of the solitons. In a recent work Katsis & Akylas (1987) have focused more thoroughly on the three-dimensional features of upstream radiation. Solving a weakly three-dimensional KdV-type equation, called the KP (Kadomtsev–Petviashvili) equation, they related the formation of two-dimensional crests to the stability of the solitary-wave solution. In a preliminary simulation they also found a wave crest becoming partly separated from a pressure field moving in an horizontally unbounded fluid. However, this calculation was carried out only for a very limited period of time. Therefore it was not possible to resolve whether the crest would become completely separated and others were to follow, or if a stationary state eventually would evolve.

Even though the presence of a surface pressure and a ship often produces similar effects, important quanitative and qualitative differences concerning wave resistance, amplitudes etc. may be expected. Karpman (1967), Mei (1976) and Mei (1986) have studied shallow-water flow round thin bodies extending throughout the water depth. In the latter work a non-homogeneous KdV equation is used to predict upstream radiation of solitons. The theory is weakly three-dimensional in the sense that variations across the channel must be sufficiently small for a cross-averaged description to be appropriate. Severe restrictions are thereby put on the shapes of the bodies. The choice of the simple, but rather unrealistic, representations of the ships is justified by assuming the blockage coefficient to be the important geometrical parameter.

Most of the theoretical studies so far have concentrated on relatively narrow channels. The present report is devoted to genuine three-dimensional wave generation in wide channels as well as an infinite medium. Strongly supercritical cases are analysed by a simplified theory related to the works of Karpman (1967) and Mei (1976), weakly supercritical cases by a fully three-dimensional set of Boussinesq equations. A simplified set of equations corresponding to the KP equation is formulated, but we have preferred to solve the Boussinesq equations because of their wider range of validity. As wave-generating forcing we have applied both a pressure distribution on the free surface and a source/sink distribution corresponding to the representation of a thin ship in Mei (1986). The analysis of wave generation by a pressure field will also apply directly to the case of a shoal in a uniform current. For finite channels our results display good agreement with the experiments of Ertekin *et al.* (1984). In the present paper much effort is put into revealing the physical mechanisms involved in upstream radiation, and we find an interpretation of the transition from three- to two-dimensional wave crests that is much further developed than the one given by Katsis & Akylas (1987). Formation of plane solitons is more closely related to the reflections at the sidewall of the channel than to the stability of two-dimensional crests. These considerations also give reason for doubting the value of the blockage coefficient as the governing parameter for wide channels. Our quantitative results support this doubt. In simulation of wave generation in unbounded sea, implementation of an effective radiation condition at the open seaward boundary enables us to carry out calculations for large time spans.

We conclude that a stationary wave pattern always emerges in unbounded sea. However, for Froude numbers sufficiently close to 1 this pattern is extended some finite distance upstream.

2. Basic equations

Weakly dispersive and nonlinear shallow-water equations have been derived in numerous articles and text books. However, inclusion of a time-dependent bottom topography corresponding to a steady flow past a shoal is not customary and we thus briefly sketch a derivation of the Boussinesq equations for this case. The equations are formulated in a coordinate system with horizontal axes ox^* and oy^* in the undisturbed water level and the vertical axis, oz^*, pointing upwards. The asterisks indicate dimensional quantities. The fluid is confined to $-h^* < z^* < \eta^*$ and the velocity potential is denoted by Φ^*. We introduce a characteristic depth h_0, wavelength l, amplitude αh_0, and dimensionless variables, according to

$$z^* = h_0 z, \quad x^* = lx, \quad y^* = ly, \quad t^* = l(gh_0)^{-\frac{1}{2}},$$
$$h^* = h_0(1+\alpha r), \quad \eta^* = \alpha h_0 \eta, \quad \Phi^* = \alpha l(gh_0)^{\frac{1}{2}}\Phi, \quad p^* = \alpha\rho g h_0 p,$$

where p^* is an external pressure applied to the surface, ρ is the density of the fluid, g is the constant of gravity and r describes the variations in the bottom topography. We note that the relative depth variations are prescribed to be of the same order as the non-dimensional amplitude α, which is assumed small.

2.1. *Formulation for the general case*

In dimensionless form the governing equations for irrotational, incompressible flow become

$$\epsilon\nabla^2\Phi = -\Phi_{zz}, \qquad -(1+\alpha r) < z < \alpha\eta, \tag{2.1}$$

$$\Phi_t + \tfrac{1}{2}\alpha(\nabla\Phi)^2 + \tfrac{1}{2}\alpha\epsilon^{-1}(\Phi_z)^2 + \eta + p = 0, \quad z = \alpha\eta, \tag{2.2}$$

$$\epsilon(\eta_t + \alpha\nabla\Phi\cdot\nabla\eta) = \Phi_z, \qquad z = \alpha\eta, \tag{2.3}$$

$$\epsilon(r_t + \alpha\nabla\Phi\cdot\nabla r) = -\Phi_z, \qquad z = -(1+\alpha r), \tag{2.4}$$

where indices denote partial differentiation, ∇ is the horizontal component of the gradient operator and $\epsilon = h_0^2/l^2$ which, according to the long-wave assumption, is small. Provided the lateral boundary conditions and the initial conditions are independent of z to zeroth order in ϵ the above equations imply

$$\Phi(x, y, z, t) = \Phi(x, y, 0, t) + O(\epsilon). \tag{2.5}$$

A depth-averaged velocity potential is defined by

$$\phi = (1+\alpha(r+\eta))^{-1} \int_{-(1+\alpha r)}^{\alpha\eta} \Phi \, \mathrm{d}z. \tag{2.6}$$

Using (2.5) and (2.6) the depth-averaged velocity can be expressed

$$\boldsymbol{v} = \nabla\phi + O(\epsilon^2, \alpha\epsilon). \tag{2.7}$$

The simplicity of this equation is crucially dependent on $(h^* - h_0)/h_0$ being of order α. From (2.7) and the requirement of volume conservation in a vertical fluid column we find

$$\eta_t + r_t = -\nabla\cdot\{(1+\alpha(r+\eta))\,\nabla\phi\} + O(\epsilon^2, \alpha\epsilon). \tag{2.8}$$

Integration of (2.1) combined with (2.3) and (2.5) gives

$$\phi = \Phi|_{z=\alpha\eta} - \tfrac{1}{2}\epsilon\eta_t - \tfrac{1}{6}\epsilon\nabla^2\phi + O(\epsilon^2, \alpha\epsilon). \tag{2.9}$$

Again the simplicity of the expression is due to the restrictions on the size of the depth variations. Eliminating η_t using (2.8) and substituting $\Phi|_{z=\alpha\eta}$ from (2.9) into the Bernoulli equation (2.2) we obtain

$$\dot{\phi} + \tfrac{1}{2}\alpha(\nabla\phi)^2 + \eta + p - \tfrac{1}{2}\epsilon r_{tt} - \tfrac{1}{3}\epsilon\nabla^2\dot{\phi} = O(\epsilon^2, \alpha\epsilon), \tag{2.10}$$

where $\dot{\phi}$ is defined as ϕ_t. The redefinitions $\tilde{\eta} = \eta + r$, $\tilde{p} = p - r - (\epsilon/2)\, r_{tt}$ will make (2.8) and (2.10) identical to what is obtained by setting $r \equiv 0$. To order $(\epsilon^2, \alpha\epsilon)$ the pressure field $\tilde{p}$ thus produces the same stationary or periodic wave pattern in the far field as the shoal. For this reason we have performed calculations only for $r \equiv 0$. The formulation of the Boussinesq equations given by (2.8) and (2.10) is the one we have preferred to solve numerically. We shall nevertheless briefly remark on a parabolized version of these equations. If the variations in the y-direction are small, all nonlinear and dispersion terms involving y-derivatives may be dropped to give

$$\eta_t + r_t \approx -\{(1 + \alpha(r+\eta))\,\phi_x\}_x - \phi_{yy}, \tag{2.11}$$

$$\dot{\phi} + \tfrac{1}{2}\alpha(\phi_x)^2 + \eta + p - \tfrac{1}{2}\epsilon r_{tt} - \tfrac{1}{3}\epsilon\dot{\phi}_{xx} \approx 0, \tag{2.12}$$

where the tildes are omitted. These equations have similar range of validity as the KP equation used by Katsis & Akylas and will provide an appropriate description of ship wave patterns for which the crests are nearly parallel to the y-axis. Equations of this type will thus become invalid for large Froude numbers and for short-crested waves in the wake if $F \sim 1$. Compared to the KP equation the set (2.11) and (2.12) is considerably simpler to solve numerically.

2.2. *The solitary-wave solution*

For a solitary wave we may write $\nabla\phi = U(x-ct)\boldsymbol{i}$, $\eta = \eta(x-ct)$, $\alpha = A$, where $\boldsymbol{i}$ is the unit vector in the x-direction and A is defined as the maximum value of η^*/h_0. Substitution into (2.8) and (2.10) followed by some standard integration gives

$$\eta = U(c - AU)^{-1}, \tag{2.13}$$

$$-\tfrac{1}{6}AU^3 + \tfrac{1}{2}cU^2 + A^{-1}U + cA^{-2}\log(1 - AU/c) = \tfrac{1}{6}\epsilon c(U')^2, \tag{2.14}$$

$$c^2 = (1+A)^2\{(1+A)\log(1+A) - A\}\{\tfrac{1}{3}A^3 + \tfrac{1}{2}A^2\}^{-1} = 1 + A + O(A^2). \tag{2.15}$$

To assure full consistency between the solitary-wave solution and the basic equations we integrate (2.14) numerically with high accuracy instead of using approximate analytical expressions.

2.3. *Boussinesq equations for the strongly supercritical case*

If an external pressure distribution of form $p = p(x-Ft)$, with $F - 1 = O(1)$, is applied to the free surface the generated wave pattern must be expected to become stationary in a reference frame following the pressure field. In such cases the field quantities can be expressed in terms of y and the new 'time' variable $\tau = t - x/F$. Mei (1976) derived general dispersive long-wave equations for this regime as well as simplified versions of more limited ranges of validity. Below we formulate a set of Boussinesq-like equations more appropriate for direct numerical solution than the

equations reported by Mei. Invoking τ and setting $r \equiv 0$ in the Bernoulli equation (2.10) and the continuity equation (2.8) we obtain

$$\phi_\tau + \tfrac{1}{2}\alpha(\phi_y)^2 + \tfrac{1}{2}\alpha F^{-2}(\phi_\tau)^2 + \eta + p - \tfrac{1}{3}\epsilon(\phi_{yy\tau} + F^{-2}\phi_{\tau\tau\tau}) = O(\epsilon^2, \alpha\epsilon), \tag{2.16}$$

$$\eta_\tau = -\{(1+\alpha\eta)\phi_y\}_y - F^{-2}\{(1+\alpha\eta)\phi_\tau\}_\tau + O(\epsilon^2, \alpha\epsilon). \tag{2.17}$$

Provided $F-1 = O(1)$ the solution at, say, $\tau = \tau_1$ is influenced only by the domain $\tau < \tau_1$ and a method involving explicit advance in τ may be formulated. Solution of (2.16) and (2.17) as an initial-value problem is however impossible because the last term in (2.16) gives rise to free wave modes with exponential growth in τ. From (2.16) and (2.17) we extract the dominant balance

$$(1-F^{-2})\phi_{\tau\tau} - \phi_{yy} + p_\tau = O(\epsilon, \alpha). \tag{2.18}$$

As long as $(1-F) = O(1) \gg O(\epsilon, \alpha)$ this equation can be used to eliminate the $\phi_{\tau\tau\tau}$ term in (2.16). The order of the equation is then reduced by introduction of the velocities $v = \phi_y$, $u = -F^{-1}\phi_\tau$ to achieve a set containing three equations for η, u, v:

$$v_\tau = -Fu_y + O(\epsilon^2, \alpha\epsilon), \tag{2.19}$$

$$\eta_\tau = F^{-1}\{(1+\alpha\eta)u\}_\tau - \{(1+\alpha\eta)v\}_y + O(\epsilon^2, \alpha\epsilon), \tag{2.20}$$

$$u - \tfrac{1}{2}\alpha F^{-1}(u^2+v^2) = F^{-1}(\eta+\hat{p}) + \tfrac{1}{3}\epsilon(1-F^{-2})^{-1}u_{yy} + O(\epsilon^2, \alpha\epsilon), \tag{2.21}$$

where the pressure term is modified according to

$$\hat{p} = p + \tfrac{1}{3}\epsilon(F^2-1)^{-1}p_{\tau\tau}. \tag{2.22}$$

Equation (2.19) is recognized as the irrotational requirement and may be replaced by the y-component of the momentum equation, which is found by differentiating (2.21) with respect to y and application of (2.19):

$$v_\tau + \tfrac{1}{2}\alpha(u^2+v^2)_y = -(\eta+\hat{p})_y + \tfrac{1}{3}\epsilon(1-F^{-2})^{-1}v_{yy\tau} + O(\epsilon^2, \alpha\epsilon). \tag{2.23}$$

The set (2.20), (2.21) and (2.23) will also describe the limiting case $F = \infty$. The equations above may also describe other problems such as normal reflection of solitons from a straight wall.

Outside a pressure field in infinite fluid we would expect to find only outgoing waves in the y-direction. In the far field the motion may therefore be described by a KdV equation as reported by Karpman (1967) and Mei (1976). The development of the wave pattern in the downstream direction will thus correspond closely with time evolution from an initial disturbance in two dimensions. The latter problem is extensively analysed by use of the inverse scattering technique. Hence, a pressure field moving with supercritical speed must be expected to create a number of divergent solitons followed by a modulated wavetrain.

3. Numerical methods

The approximation to a quantity f at a gridpoint with coordinates $(\beta\Delta x, \gamma\Delta y, \kappa\Delta t)$ where Δx, Δy and Δt are the grid increments, is denoted by $f^{(\kappa)}_{\beta,\gamma}$. To improve the readability of the difference equations we introduce the symmetric difference operator δ_x:

$$\delta_x f^{(\kappa)}_{\beta,\gamma} = \frac{1}{\Delta x}(f^{(\kappa)}_{\beta+\frac{1}{2},\gamma} - f^{(\kappa)}_{\beta-\frac{1}{2},\gamma}), \tag{3.1}$$

and the midpoint average operator $^{-x}$:

$$(\bar{f}^x)^{(\kappa)}_{\beta,\gamma} = \tfrac{1}{2}(f^{(\kappa)}_{\beta-\frac{1}{2},\gamma} + f^{(\kappa)}_{\beta+\frac{1}{2},\gamma}). \tag{3.2}$$

Difference and average operators with respect to the other coordinates y and t are defined correspondingly. We note that all combinations of these operators are commutative. To abbreviate the expressions further we also group terms of identical indices inside square brackets, leaving the super- and subscripts outside the bracket.

3.1. *Numerical integration of the full Boussinesq equations*

For the set (2.8), (2.10) we use a grid staggered in time only, calculating the quantities $\eta^{(n)}_{i,j}$, $\dot{\phi}^{(n)}_{i,j}$ and $\phi^{(n+\frac{1}{2})}_{i,j}$. According to the discussions in §2.1 we set $r \equiv 0$. The difference equations read

$$[\delta_t \eta = -\delta_x\{(1+\alpha\bar{\eta}^{x,t})\,\delta_x\phi\} - \delta_y\{(1+\alpha\bar{\eta}^{y,t})\,\delta_y\phi\} - \tfrac{1}{12}(\Delta x^2+\Delta y^2)\,\delta_x^2\,\delta_y^2\,\phi]^{(n-\frac{1}{2})}_{i,j}, \tag{3.3}$$

$$[\dot{\phi} + T + \eta + \hat{p} - \{\tfrac{1}{3}\epsilon + \tfrac{1}{12}(\Delta t^2 - \Delta x^2)\}\,\delta_x^2\,\dot{\phi} - \{\tfrac{1}{3}\epsilon + \tfrac{1}{12}(\Delta t^2 - \Delta y^2)\}\,\delta_y^2\,\dot{\phi} = 0]^{(n)}_{i,j}, \tag{3.4}$$

where
$$\hat{p} = p + \tfrac{1}{12}\Delta t^2 p_{tt} \tag{3.5}$$

and
$$[T^{(n)} = \tfrac{1}{2}\alpha\{(\delta_x\bar{\phi}^x)^{(n-\frac{1}{2})}\,(\delta_x\bar{\phi}^x)^{(n+\frac{1}{2})} + (\delta_y\bar{\phi}^y)^{(n-\frac{1}{2})}\,(\delta_y\bar{\phi}^y)^{(n+\frac{1}{2})}\}]_{i,j}. \tag{3.6}$$

In addition we have the kinematic relation

$$[\delta_t\phi = \dot{\phi}]^{(n)}_{i,j}. \tag{3.7}$$

The explicit appearance of the grid increments in (3.3)–(3.5) is due to the introduction of correction terms to the scheme obtainable by straightforward term-by-term midpoint discretization of (2.8) and (2.10). If the grid increments are comparable with the depth, the dimensionless quantities Δx, Δy and Δt become $O(\epsilon^{\frac{1}{2}})$. Hence the correction terms may be comparable with the dispersion terms and a simple midpoint scheme will be inaccurate. Inclusion of the correction terms will, on the other hand, reduce the discretization error in η to the same order as the error in the Boussinesq equations themselves. This is demonstrated by ignoring nonlinearities and dispersion terms in (3.3)–(3.5) and eliminating ϕ from the resulting equations to obtain

$$[\delta_t^2\eta = (\delta_x^2+\delta_y^2)(\eta+p) + \tfrac{1}{12}(\Delta t^2-\Delta x^2)\,\delta_x^4(\eta+p) + \tfrac{1}{12}(\Delta t^2-\Delta y^2)\,\delta_y^4(\eta+p) + \tfrac{1}{6}\Delta t^2\delta_x^2\,\delta_y^2(\eta+p) + \tfrac{1}{12}\Delta t^2(\delta_x^2+\delta_y^2)p_{tt} + O(\Delta x^4, \Delta y^4, \ldots)]^{(n)}_{i,j},$$

which is a fourth-order scheme for the linearized hydrostatic equations. Second-order errors will thus be introduced through nonlinear and dispersion terms only and the discretization error for η will be $O(\Delta x^4, \ldots, \alpha\Delta x^2, \epsilon\Delta x^2, \ldots)$ which equals $O(\epsilon^2, \alpha\epsilon)$ provided $\Delta x, \Delta y, \Delta t = O(\epsilon^{\frac{1}{2}})$. A corresponding high accuracy is not to be expected for the velocity potential ϕ.

The advance from $t = n\Delta t$ to $t = (n+1)\Delta t$ is performed through three steps: calculate $\phi^{(n+\frac{1}{2})}$ from the kinematic relation (3.7), solve the implicit equations for $\eta^{(n+1)}$ defined by (3.3) and complete the computational cycle by solving the discrete Bernoulli equation for $\dot{\phi}^{(n+1)}$. The continuum equation (3.3) gives strongly diagonal dominant coefficient matrices provided the velocities, $\delta_x\phi$ and $\delta_y\phi$, are much less than 1. Hence we apply a simple point-by-point iteration scheme for which a new generation of approximations is obtained by substitution of values from the old generation into the right-hand side of (3.3). This procedure assures conservation of volume and 5–6 iterations will generally suffice when values from the previous time step are used for initialization. For the discrete Bernoulli equation (3.4) the diagonal

dominance is too weak for a pointwise iteration procedure to be efficient. Instead an alternating direction implicit (ADI) method is used: sweeps in the x-direction, with implicit representation of terms not involving differentiation with respect to y, alternate with corresponding sweeps in the y-direction. If smoothed values from the previous time step are used for initialization two iterations will suffice in most cases. If the parabolized equations (2.11) and (2.12) are discretized in the above manner both the continuity and the Bernoulli equation give one tridiagonal equation for each row of the grid parallel to the x-axis and no iteration is needed. However, within the range of validity for (2.11) and (2.12) one iteration will suffice for solution of (3.4). In addition the time step often has to be reduced for the discretized versions of (2.11) and (2.12) owing to the weaker implicitness inherent in these equations. The reduction in CPU time will thus not be larger than 25–50 %. A numerical scheme similar to the present one has been applied to a set of Boussinesq equations valid for depth variations of order one by Pedersen & Rygg (1987). Most of their analysis and tests concerning stability, convergence etc. are relevant also in the present context. The stability criterion for the linearized difference scheme without correction terms reads

$$\Delta t^2 < \left(\frac{1}{\Delta x^2}+\frac{1}{\Delta y^2}\right)^{-1}+\tfrac{4}{3}\epsilon,$$

which is less restrictive than the standard Courant condition. Favourable choices for Δt are thus often enabled (ratio $\Delta x/\Delta t$ close to a phase velocity etc.). The corrected scheme is also slightly superior with respect to stability.

3.2. *Solution of the simplified equations by downstream marching*

Solution of the equations valid for $F-1 = O(1)$ will demand neither considerable computer time nor storage. The computational domain may thus be chosen large enough for radiation conditions to be superfluous. Again we use a staggered grid to calculate the quantities $\eta_i^{(n)}, u_i^{(n)}, v_{i+\frac{1}{2}}^{(n+\frac{1}{2})}$ where the sub- and superscripts correspond to the values of y and τ respectively. Discrete versions of (2.20) and (2.21) read

$$[\delta_\tau\{\eta-F^{-1}(1+\alpha\eta)u\} = -\delta_y\{(1+\alpha\bar{\eta}^{y,\tau})v\}]_i^{(n-\frac{1}{2})}, \tag{3.8}$$

$$\left[u-\tfrac{1}{2}\alpha F^{-1}(u^2+\hat{v}^2) = F^{-1}(\eta+\hat{p})+\frac{\epsilon F^2}{3(F^2-1)}\delta_y^2 u\right]_i^{(n)}, \tag{3.9}$$

where
$$[\hat{v}^2]_i^{(n)} = [(\bar{v}^x)^{(n-\frac{1}{2})}\{(\bar{v}^x)^{(n-\frac{1}{2})}-F\Delta\tau\delta_y(\bar{u}^x)^{(n)}\}]_i. \tag{3.10}$$

Assuming that $u^{(n-1)}$, $\eta^{(n-1)}$ and $v^{(n-\frac{1}{2})}$ are already calculated, (3.8) and (3.9) give a '7-diagonal nonlinear' set of equations for $u_i^{(n)}$ and $\eta_i^{(n)}$. The nonlinear terms are comparatively small and the set is thus easily solved by a simple iterative technique. A discretized version of (2.23) reads

$$[\delta_\tau v+\delta_y\{\tfrac{1}{2}\alpha(u^2+\hat{v}^2)+\eta+\hat{p}\} = \frac{\epsilon F^2}{3(F^2-1)}\delta_y^2\delta_\tau v]_{i+\frac{1}{2}}^{(n)}, \tag{3.11}$$

where
$$[\hat{v}^2]_{i+\frac{1}{2}}^{(n)} = [(\bar{v}^x)^{(n-\frac{1}{2})}(\bar{v}^x)^{(n+\frac{1}{2})}]_{i+\frac{1}{2}}.$$

This equation defines a set of linear tridiagonal equations for $v^{(n+\frac{1}{2})}$. Provided $F \neq \infty$ (3.11) may be replaced by a discretized version of (2.19):

$$[\delta_\tau v = -F\delta_y u]_{i+\frac{1}{2}}^{(n)}. \tag{3.12}$$

Setting $F = 0$, $F^{-1}u \equiv 0$, (3.8) and (3.11) become a scheme for the two-dimensional Boussinesq equations. This scheme is identical to a scheme obtained from the two-

dimensional versions of (3.3) and (3.4) by omitting the correction terms, applying the difference operator δ_y to the Bernoulli equation and finally recognizing the quantity $\delta_y \phi$ as v. After linearization the stability criterion for (3.8) and (3.9) combined with either (3.11) or (3.12) becomes

$$\Delta t^2 \leqslant (1-F^{-2})\Delta y^2 + \frac{4\epsilon}{3(1-F^{-2})}$$

and a favourable ratio between the grid increments is given by $\Delta t = (1-F^{-2})^{\frac{1}{2}}\Delta y$.

4. Results

4.1. *Computational domain and boundary conditions*

The scaling introduced in §2 is based on characteristic wavelengths and amplitudes for which there are a variety of different options. This procedure of scaling is convenient for derivation and discussion of the equations, but will often tend to obscure quantitative results. To increase the readability of figures and tables, we thus define a new scaling where the length unit corresponds to the equilibrium depth and the time unit corresponds to the time elapsed while covering a distance equal to one depth with the linear shallow-water speed. The new non dimensional quantities are given by

$$x' = \frac{x^*}{h_0}, \quad y' = \frac{y^*}{h_0}, \quad t' = \frac{(gh_0)^{\frac{1}{2}}t^*}{h_0}, \quad \eta' = \frac{\eta^*}{h_0}, \quad \phi' = \frac{\phi^*}{h_0(gh_0)^{\frac{1}{2}}}, \quad p' = \frac{p^*}{\rho g h_0}.$$

In the remainder of this section the primes are omitted.

All definitions and discussions in this subsection are done with regard to the fully time-dependent Boussinesq equations (2.8) and (2.10). Throughout §4 we assume either a pressure field or a source distribution along the x-axis, moving in the positive x-direction with a constant velocity which, in the present scaling, equals the Froude number. We restrict ourselves to the study of symmetric geometries and confine the computational domain to $x_0 < x < x_0 + S$, $-b_a < y < 0$, where $y = 0$ corresponds to the symmetry line of the channel and $y = -b_a$ to a sidewall or an open boundary. At intervals the computational window is shifted in the positive x-direction to prevent any part of the wave system reaching the upstream boundary. At the downstream boundary, points are correspondingly excluded from the domain causing a local distortion of the solution. This disturbance will however not be noticeable further upstream unless the Froude number is considerably less than 1. The numerical integration is always started from rest at $t = 0$. All reported calculations are performed with grid increments Δx, Δy and Δt close to unity. Estimations based on grid refinement tests and simulation of solitary-wave propagation prove this discretization to be sufficiently accurate. As an example we observe relative errors of order 2% for cases giving waves of height 0.3 depths ($\alpha \sim 0.3$).

For convenience we have selected simple analytical expressions for the pressure fields and source distributions:

$$p(x, y, t) = p_a Y\left(\left\{\left(\frac{x-Ft-x_1}{L}\right)^2 + \left(\frac{y-y_0}{R}\right)^2\right\}^{\frac{1}{2}}\right), \tag{4.1a}$$

$$\phi_y(x, 0, t) = -q\frac{\partial}{\partial t} Y\left(\frac{(x-Ft-x_1)}{L}\right). \tag{4.1b}$$

The function Y is defined by

$$\left.\begin{aligned} Y(\theta) &= \tfrac{1}{2}(1+\cos\pi\theta) \quad \text{for } |\theta| < 1, \\ Y(\theta) &= 0 \quad \text{for } |\theta| > 1. \end{aligned}\right\} \tag{4.2}$$

Equation (4.1*a*) defines a continuously differentiable pressure field having elliptic isobars and attaining a maximum value, p_a, at the moving point $x = x_1 + Ft$, $y = y_0$. Except for the case described in §4.4 we always have $y_0 = 0$. The normal velocity (4.1*b*) corresponds approximately to a thin, moving body defined by $y = -qY$ and gives a continuous and sinusoidal (one period) sink/source distribution. Naturally the integrated effects of this distribution depend on the surface level at the boundary. In the absence of a flux through the boundary $y = 0$ a symmetry condition is applied to assign values to the fictitious quantities at $y = \frac{1}{2}\Delta y$. If a normal velocity is specified we use (4.1*b*) and

$$\eta_y = (1 + O(\epsilon, \alpha))\, qY_{tt}, \tag{4.3}$$

which follows from the Bernoulli equation (2.10). When fictitious values obtained by (4.3) are substituted into the discretized continuity equation relative errors of order $(\alpha\epsilon, \alpha^2)$ are introduced and the overall accuracy of the model is maintained. For channels of finite width, b, a symmetry condition is applied to the boundary $y = -b_a = -b$. In the case of an infinite fluid we have to deal with an open boundary. Formulation of correct radiation conditions for nonlinear problems is generally very difficult. In the present case this task is substantially simplified because the system of outgoing waves consists of a series of recognizable wave crests which become completely separated provided the distance from the disturbance is large enough. At $y = -b_a$ we may thus apply a radiation condition of the Sommerfeldt type:

$$\left\{\frac{\partial}{\partial t} - \frac{c(x,t)}{\sin\psi(x,t)}\frac{\partial}{\partial y}\right\}(\phi, \eta) = 0, \tag{4.4}$$

where c is the phase velocity and ψ is the angle between the direction of wave advance and the x-axis. Using spline interpolation the quantities c and ψ are found for each wave crest in the vicinity of the open boundary. The radiation condition cannot be expected to be effective unless the distance b_a is large enough for the crests to be separated and to display sufficiently slow variations with respect to shape, speed and orientation. We note that, apart from errors due to discretization and interpolation, a solitary wave will be treated exactly by the procedure described above. Accurate calculations of ψ and c demand that interpolation is performed for a large portion of the domain adjacent to the boundary, particularly for relatively coarse grids. As a compromise between accuracy and CPU time usage we have settled for extending the interpolation throughout a 15-point-wide band following the boundary. Testing indicates that introduction of errors of up to 2–3% sometimes may be expected for this choice. Channels of finite width with absorbing lateral boundaries may also be described by implementation of a radiation condition.

We define the blockage coefficients by

$$B = \frac{\frac{1}{2}p_a R}{b}, \quad B = \frac{q}{b} \tag{4.5}$$

for the source and pressure distributions respectively. The wave resistance experienced by a pressure field is given by

$$C_x \boldsymbol{i} + C_y \boldsymbol{j} = -\int\int p \nabla\eta \, \mathrm{d}x \, \mathrm{d}y, \tag{4.6}$$

and the net momentum flux associated with a source distribution is

$$I_x \boldsymbol{i} + I_y \boldsymbol{j} = \int (1+\eta) q Y_t \nabla\phi(x, 0, t)\, \mathrm{d}x, \tag{4.7}$$

where $\boldsymbol{i}$ and $\boldsymbol{j}$ denotes unit vectors in the x- and y-direction respectively. In the latter case $-I_x$ is interpreted as the wave resistance.

4.2. *Upstream waves in wide channels*

In their experiments Ertekin *et al.* (1984) observed upstream radiation in channels with half-width 24.4 depths and blockage coefficient 0.019. In subsequent paper Ertekin *et al.* (1986) report on numerical calculations for channels of half-width 4, which is too small to reveal the mechanisms for generation of two-dimensional solitons in a genuine three-dimensional geometry. Katsis & Akylas (1987) performed simulations in wider channels where this transition is clearly visible. In addition they made a study of the evolution of free, laterally non-uniform crests in a channel and concluded that a stable two-dimensional soliton develops through interactions with the sidewalls. However, they addressed this wall effect merely by a vague reference to diffraction.

We shall compare our theoretical results to the measurements of Ertekin *et al.* concerning their largest channel width, and perform calculations for different combinations of parameter values, to examine the importance of the blockage coefficient and channel width. We have combined the three half-widths $b = 10$, 20, 40 with three different pressure and source distributions, which are denoted by (i), (ii), (iii) and described in table 1.

Different stages during the development of the wave patterns for pressure field (i) and the two Froude numbers 1.4 and 1.05 are depicted in figure 1. For $F = 1.4$ the diverging waves rapidly form a stationary criss-cross pattern through reflections from the sidewalls. Regarding the build-up of the leading diverging wave for $F = 1.05$ the most striking feature is perhaps that no more than scarcely visible reflection is ever present. Instead a high stem perpendicular to the wall is created and continuously catches up with the diverging wave until an almost purely plane wave is formed. This is clearly the phenomenon called Mach reflection as described by Wiegel (1964), Miles (1977*a*, *b*), Melville (1979) and Funakoshi (1980). During the growth of the stem the part of the wave crest at the centreline of the channel slowly outruns the pressure field, indicating that the leading diverging wave may also leave the pressure field in the absence of a sidewall. We note that the Mach-stem effect not only straightens the leading diverging wave but also causes a growth of the amplitude which, according to (4.6), increases the wave resistance and speeds up the separation from the pressure field. Thus, except for extremely wide channels, soliton radiation cannot be described as the two separate events of emission from the pressure field and straightening of the crests caused by the channel walls. The Mach stem playing such a dominant part during upstream radiation makes it less likely that the blockage coefficient is the only essential geometrical parameter. With exception of the neighbourhood of the pressure, comparison of surface profiles to the exact solitary wave, given by (2.13)–(2.15), shows deviations hardly exceeding expected discretization errors by the last stages depicted in figure 1*c*. After a crest has left the pressure field, it very quickly attains the shape of a solitary wave throughout its width. After a few solitons are generated the emission becomes regular and a uniform train of solitons is produced. Upstream radiation also occurs for $F < 1.0$ but in this case the amplitude decreases for each soliton generated and no

	Pressure			Source	
	p_a	R	L	q	L
(i)	0.1	10	12	0.5	12
(ii)	0.05	10	12	0.25	12
(iii)	0.05	5	12	0.125	12
(E)	0.1147	10	12	0.5734	12

TABLE 1. Source and pressure distributions

state of periodic emission is achieved. This is in agreement with earlier results for narrow channels (Wu & Wu 1982; Mei 1986).

The pressure and source distributions denoted by (E) in table 1 are intended to correspond to the case $b^* = 244$ cm, $h^* = 10$ cm and $B = 0.0235$ from Ertekin *et al.* This means that the blockage coefficients and channel widths are equal and that the lengths of the disturbances are of roughly the same size. From their sketches of the experimental set-up and the time histories at fixed wave gauges it may be deduced that the last wave gauge is located approximately 230 depths upstream relative to the initial position of moving vessel and midway between the symmetry line and the sidewall of the channel. This distance seems, however, to vary slightly from one experiment to another and is not explicitly defined or tabulated. Ertekin *et al.* reports the height of the leading soliton that will also emerge for subcritical Froude numbers. We shall denote this amplitude by A_{230}. According to our theoretical results the leading crest is still developing at $x = 230$, especially for the larger Froude numbers, and the uncertainties regarding the gauge locations may thus cause noticeable deviations. Nevertheless, with the exception of $F = 1.15$, both sets of computed A_{230} agree excellently with the experiments, as shown in figure 2(*a*). For high Froude numbers we find significant differences between A_{230} and the amplitudes of both leading and periodically generated solitons at $x = \infty$. Experimental determination of the period of soliton generation is difficult because of the limited sizes of the laboratory wave tanks. Ertekin *et al.* do report measurements of a quantity denoted by T_m which might give an indication of the value of the period relative to a reference frame following the disturbance. The definition of T_m reads

$$T_m = \frac{\bar{c}}{\bar{c}-F} T_f,$$

where T_f is the time elapsed between the two first maxima at $x = 230$ and $\bar{c}$ is the averaged wave celerity for the leading crest between the two last gauges. Because the difference $\bar{c}-F$ is small, T_m is very sensitive to even minor alterations in wave speeds, gauge locations etc. Against this background the agreement between theoretical and experimental T_m, as depicted in figure 2(*b*), must be regarded as satisfactory. No proper theoretical estimation of T_f for $F = 1.15$ is possible because the second wave crest is insufficiently developed. Anyway, for the higher Froude numbers the second wave is not yet separated from the disturbance at $x = 230$ and its appearance at this stage may depend on details concerning the initial conditions etc. (see also discussion in Mei 1986).

Amplitude A and period T for the generated train of solitons are displayed in figure 3 for $b = 10$, 20, 40 combined with different disturbances from table 1. The period T is defined relative to a frame of reference at rest. For the highest Froude numbers

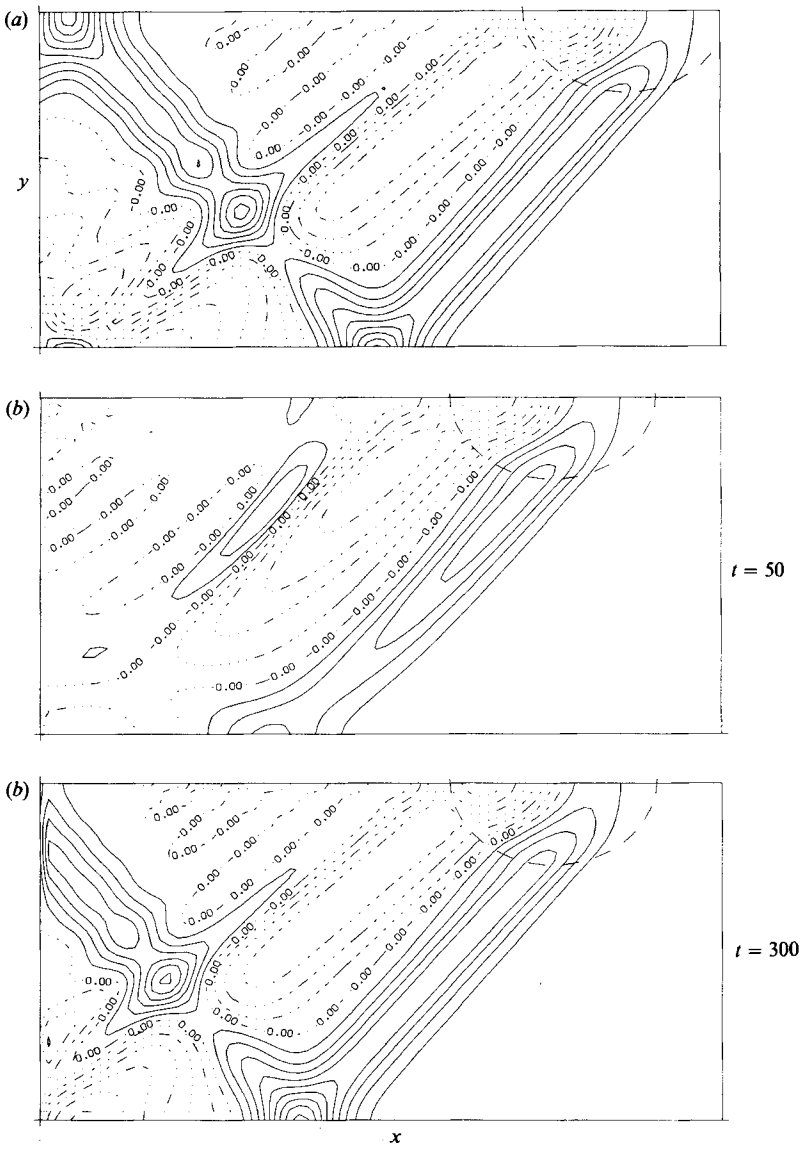

FIGURE 1 (*a–b*). For caption see facing page.

allowing upstream radiation we find amplitudes too large for the Boussinesq equations to provide quantitatively good results. It is thus not considered worthwhile estimating accurate upper limits for F, denoted by F_u, for the radiative regime. Upper and lower bounds for F_u are, however, given in table 2. The results in figure 3 confirm earlier observations that the blockage coefficient B determines the amplitude of the radiated solitons. The period is, on the other hand, not particularly related to B and the limit F_u shows no clear dependence on B. Keeping B fixed we find that the period decreases with the half-width b as shown in figure 4. Both amplitude and period increase monotonically with the Froude number. From estimation of wave speeds in the numerical simulations it is found that the difference in speed between the radiated waves and the moving disturbance does not tend to zero when F approaches

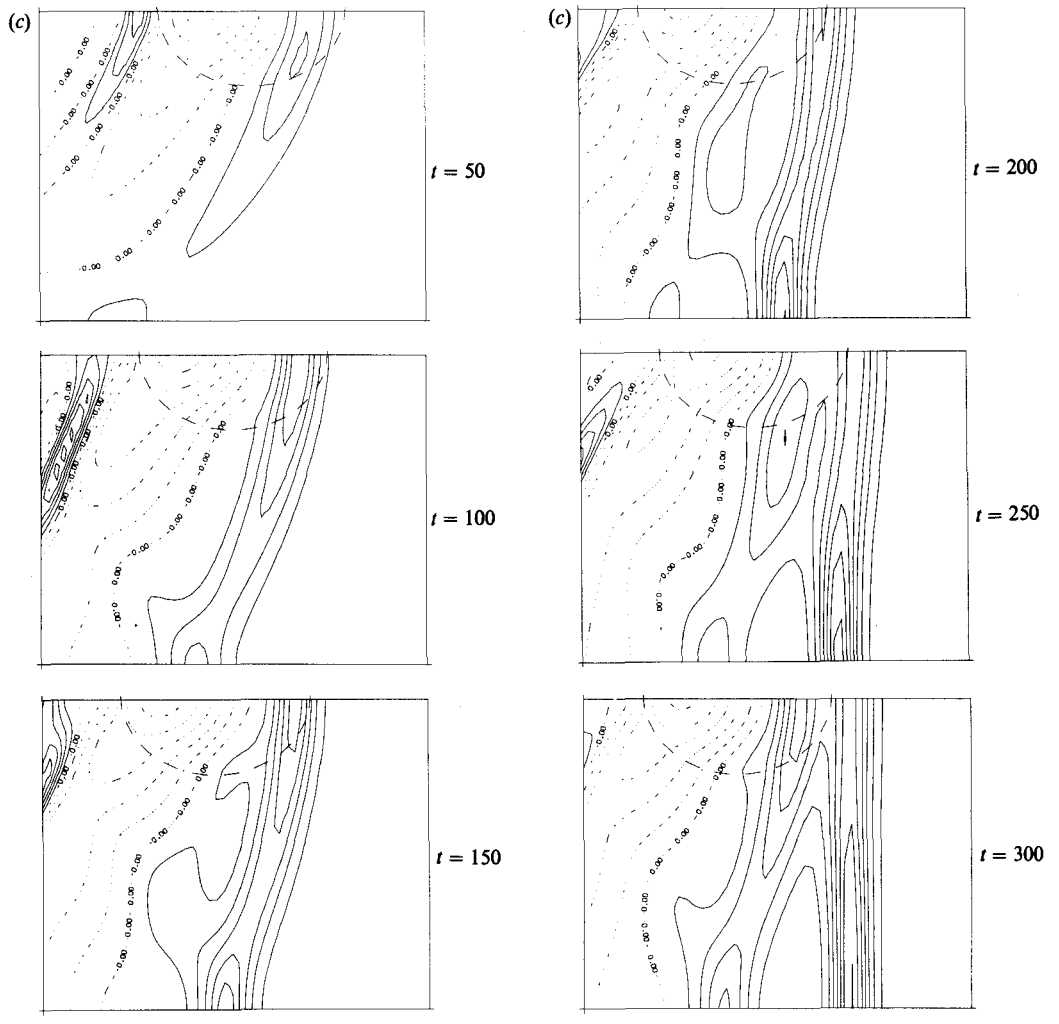

FIGURE 1. Contour plots of the surface elevation at different values of t for pressure field (i) (see table 1) and $b = 40$. The dashed semicircles indicate the locations of the pressure fields. Solid lines show positive contour lines. (*a*) $F = 1.4$, equations (2.20)–(2.23), contour interval = 0.02. (*b*) $F = 1.4$, full Boussinesq equations, contour interval = 0.02. (*c*) $F = 1.05$, full Boussinesq equations, contour interval = 0.04. Only a length of 50 depths of a total of $S = 80$ is displayed. The symmetry line and the sidewall of the channel correspond to the upper and lower horizontal lines respectively.

F_u. This is different for the stronger nonlinear cases reported by Ertekin *et al.* for which the amplitudes eventually reach the theoretical maximum for solitary waves. To explain this behaviour we have to study in some detail the reflections occurring at the sidewalls and the interaction between the Mach stem and the disturbance which are described at the beginning of this subsection. First, F_u is related to the largest Froude number for which the leading diverging wave produced by the disturbance in an unbounded sea would be subjected to Mach reflection at a wall parallel to the x-axis. Even though the discussion of waves in a horizontally unbounded fluid belongs to the next subsection we thus make a preliminary study concerning pressure field (ii) in this case. For F larger than 1.1, say, we do not observe

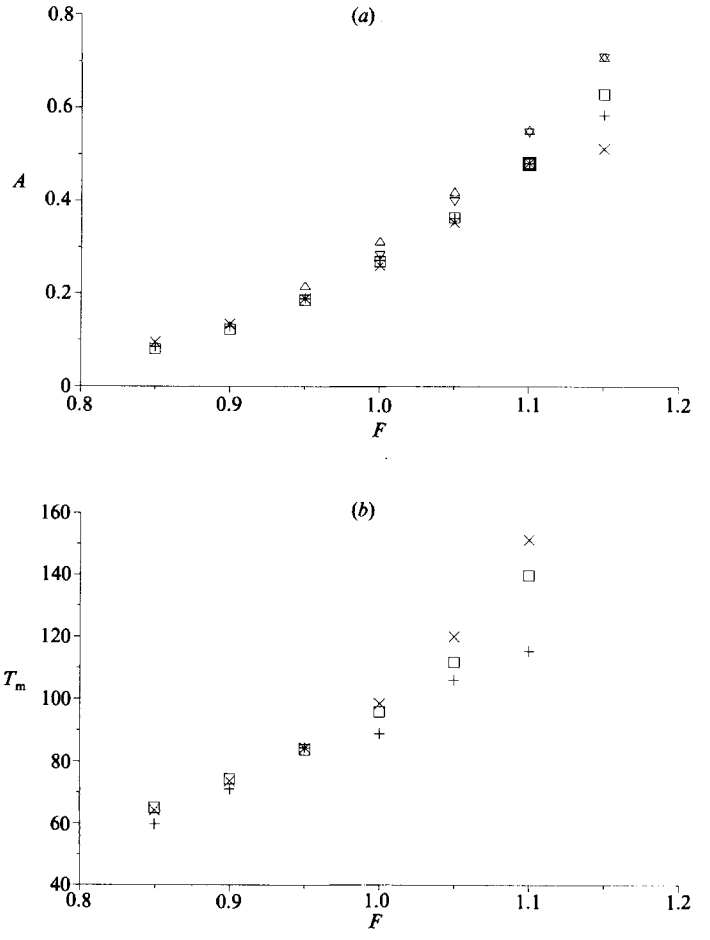

FIGURE 2. (*a*) Amplitude versus Froude number: +, measurements of A_{230} from Ertekin *et al.* for the case $b^* = 244$ cm, $h^* = 10$ cm; ×, A_{230} for $b = 24.4$ and pressure with $R = 10$, $L = 12$, $p_a = 0.1147$; □, A_{230} for $b = 24.4$ and source with $L = 12$, $q = 0.573$; △, amplitude of the leading soliton as $x \to \infty$ for the source; ▽, amplitude of the periodic solitons generated by the source. In all cases we have $B = 0.0235$. For $F = 1$ it is uncertain whether a periodic state is reached or not. (*b*) The 'period' T_m versus Froude number. Symbols as for (*a*).

any noticeable upstream influence of pressure (ii) moving in an unbounded sea. In figure 5 we have depicted the amplitude A and the angle ψ between the x-axis and the direction of wave advance for the leading diverging wave at a distance corresponding to $y = -b = -20$. Above $F \sim 1.11$, $A(F)$ and $\psi(F)$ are slowly varying functions; in the neighbourhood of $F = 1.1$ abrupt variations clearly indicating some qualitative changes in the solutions do however occur. The discussion of this feature is postponed to the next subsection. Predictions, based on the present theory, of the critical angle for transition to Mach reflection of solitons give $\psi_c = 20.3°$ for $A = 0.05$ and $\psi_c = 26.9°$ for $A = 0.1$ (see the Appendix). Therefore, Mach reflection will probably occur for $F = 1.125$ ($A = 0.091$, $\psi = 23.3°$) but not for $F = 1.15$ ($A = 0.077$, $\psi = 27.2°$), which is consistent with the result $1.125 < F_u < 1.15$ from table 2. We now return to describing the finite-width channel. When the Mach stem extends into the pressure field a sharp increase in wave resistance takes place (see figure 6) which

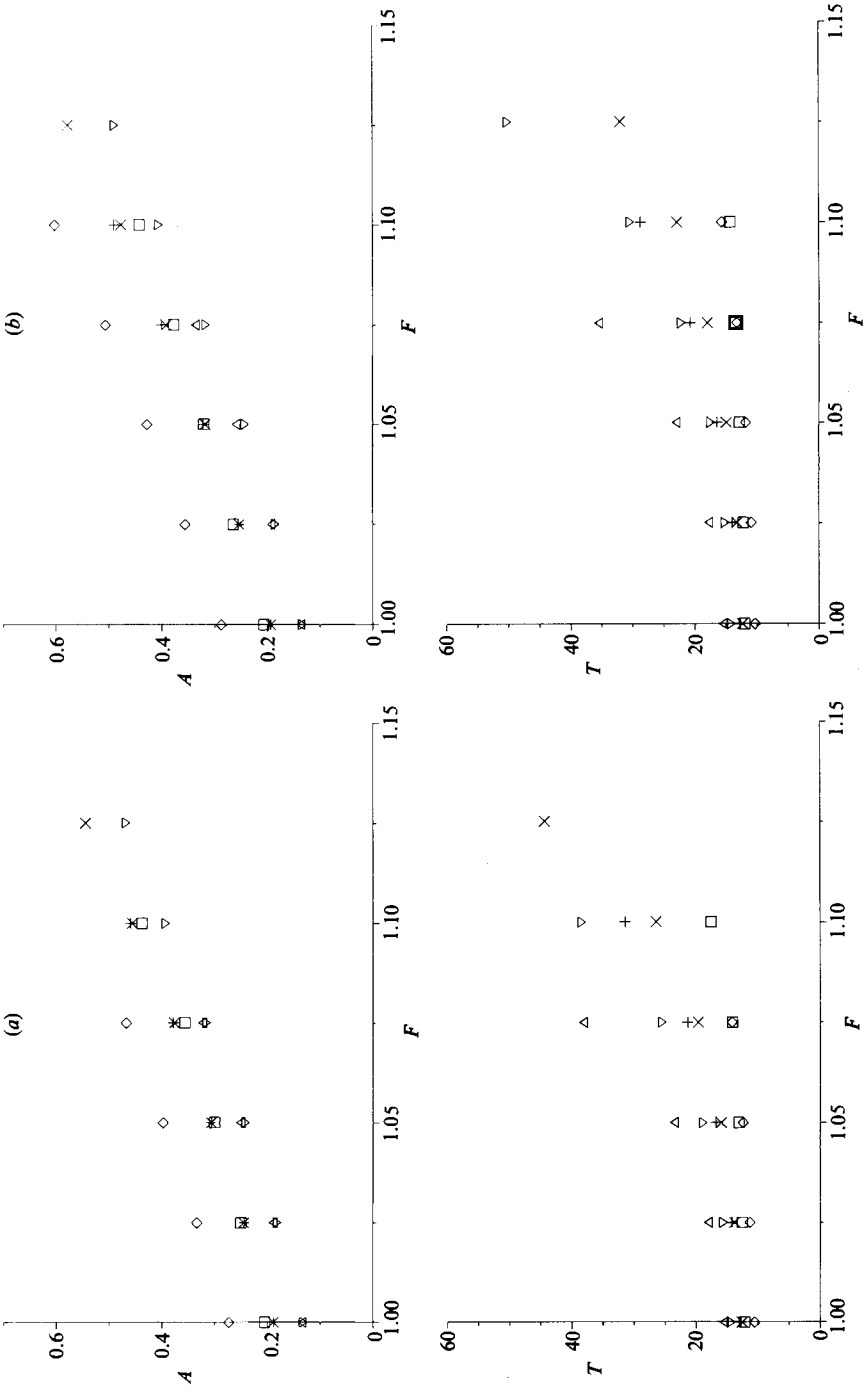

FIGURE 3. Amplitudes and periods for a train of upstream solitons: (*a*) pressure field, (*b*) source distribution. △, $b = 20$ and (iii); ▽, $b = 40$ and (ii), +, $b = 10$ and (iii); ×, $b = 20$ and (ii); □, $b = 40$ and (i); ◇, $b = 10$ and (ii). The first two both give $B = 0.00625$ and the next three give $B = 0.0125$. The roman numbers refer to the disturbances listed in table 1.

b	(i)	(ii)	(iii)	Disturbance
10	—	$1.150 < F_u < 1.200$	$1.100 < F_u < 1.125$	Pressure
20	—	$1.125 < F_u < 1.150$	$1.075 < F_u < 1.100$	Pressure
40	$1.150 < F_u < 1.200$	$1.125 < F_u < 1.150$	$1.075 < F_u < 1.100$	Pressure
10	—	$1.150 < F_u < 1.200$	$1.250 < F_u < 1.500$	Source
20	—	$1.150 < F_u < 1.160$	$1.075 < F_u < 1.100$	Source
40	$1.150 < F_u < 1.200$	$1.250 < F_u < 1.150$	$1.075 < F_u < 1.100$	Source

TABLE 2. Critical Froude numbers for upstream radiation

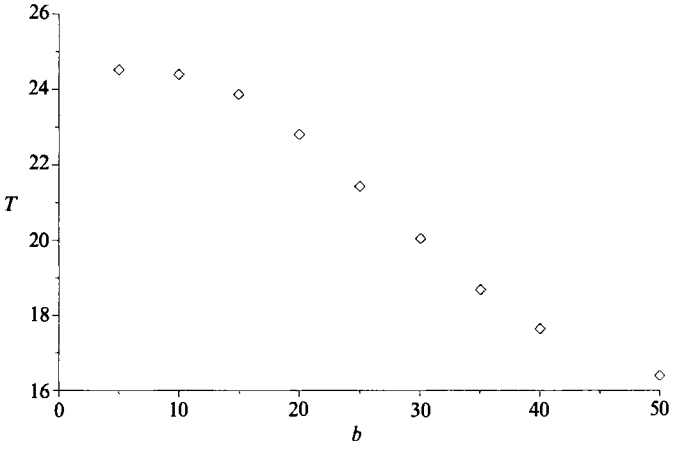

FIGURE 4. Period T for an upstream wavetrain as function of the half-width b, for fixed $B = 0.00625$.

causes further amplification and thereby an increase in the wave speed. This amplification will be most pronounced for the highest Mach stems, which occur for inclinations close to ψ_c. Therefore the speed of the radiated waves relative to the disturbance will not tend to zero in the limit $F \to F_u^-$. These effects explain the very high amplitudes observed for Froude numbers close to F_u. From the above discussion it also follows that F_u for wide channels will vary slowly with b and may approach a limit different from 1 when $b \to \infty$.

4.3. *Wave patterns in an unbounded sea*

As noted in §4.2 the graphs in figure 5 give evidence that some sort of regime transition occurs near $F = 1.1$ for pressure (ii) in an unbounded sea. A more detailed investigation of the wave fields shows that the sudden increase in amplitude of the leading wave as F is decreased toward 1.1 is accompanied by a forward shift of its position relative to the pressure field. A second diverging wave originating from the former part of the pressure field also appears. At some lower Froude number this pattern is repeated and a second wave crest is moved into an upstream position. Wave patterns for $F = 1.11$, 1.09 and 1.05 are displayed in figures 7–9. For all cases investigated, a stationary wave pattern with a finite number of wave crests located upstream is reached for large t. The time span needed to develop a steady state is large, however, often corresponding to moving the pressure field some thousands of depths.

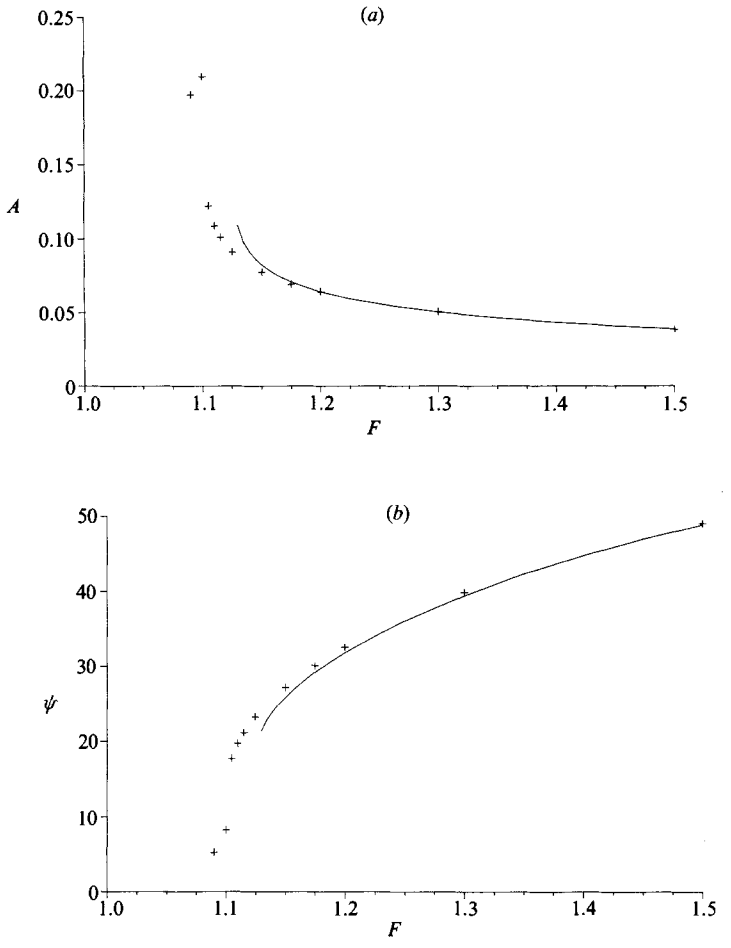

FIGURE 5. Amplitude A and orientation ψ at $y = -20$ for the leading divergent wave produced by pressure field (ii) in an infinite medium. The lines correspond to the solution of equations (2.20)–(2.23), the 'plus' marks to results obtained by the full Boussinesq equations.

At the symmetry line ahead of the pressure field the upstream crests are situated close to each other and their heights decrease in the upstream direction. As we move toward the open boundary the height variation is reversed and the distances between the crests increase. For large y the system is split into a sequence of completely separated straight-crested solitons. Generally the upstream waves are followed by at least one crest originating from within the disturbance that also attains the shape of a soliton. The hindmost upstream wave remains in contact with the pressure field to give an input of momentum and energy which counterbalances the total lateral radiation in the upstream domain. The upstream transport of these quantities is probably achieved by the same sort of mechanisms that govern the collision and momentum exchange between two slightly different unidirectional solitons. Ahead of the pressure field the crests are well within 'collision range' for solitons of corresponding heights and the shape of every upstream wave resembles the shape of a soliton. Some qualitative deviation does appear at the tail of the hindmost crest which is directly influenced by the pressure field. This is however irrelevant as far as the interaction between the crests is concerned. The amplitude decrease in the positive

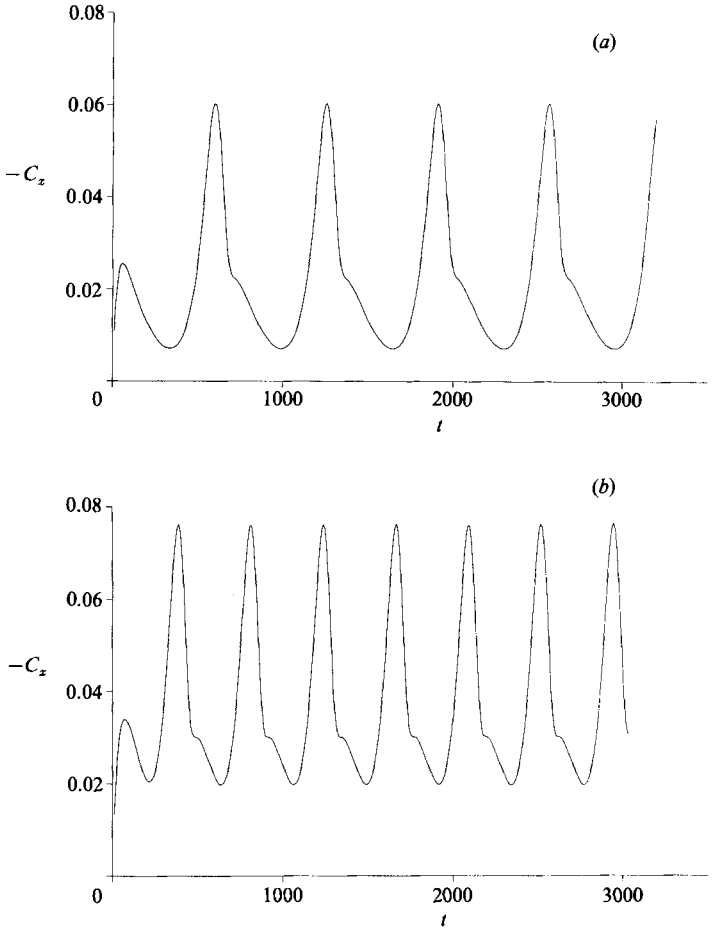

FIGURE 6. The wave resistance C_x for $F = 1.125$, $b = 20$ and (a) pressure (ii), (b) source (ii).

x-direction clearly indicates an upstream transport of energy and momentum. As an example we consider the two upstream crests for $F = 1.05$ and pressure (ii) (figure 9). At $y = 0$ these waves have heights 0.114 and 0.134 respectively and are separated by a distance $d = 10.81$. If two unidirectional solitons of amplitudes 0.1 and 0.16 collide the exchange of momentum and energy occur for d less than, say, 15 and larger than 9.9, which is the closest the two crests ever get. At one intermediate stage we find two peaks of amplitudes 0.113 and 0.136 separated by a distance $d = 10.3$. The collision is analysed by numerical integration of the Boussinesq equations (2.8) and (2.10) for the two-dimensional case. As shown in figures 7–9 a third soliton-shaped crest appears in addition to the two discussed above. This is however an 'ordinary diverging soliton' and does not count as an upstream wave. Nevertheless, according to figure 7 (c, d) this wave may, at least to some extent, contribute to the upstream energy tranport through interactions with the hindmost upstream wave.

Table 3 contains the number of upstream waves produced by different combinations of pressure fields and Froude numbers. Some results for a moving source are also displayed in the table. Again a source and a pressure field give rise to very similar effects. One might suspect that the generation of a crest ahead of the disturbance is due to an imperfection of the radiation condition. However, alteration

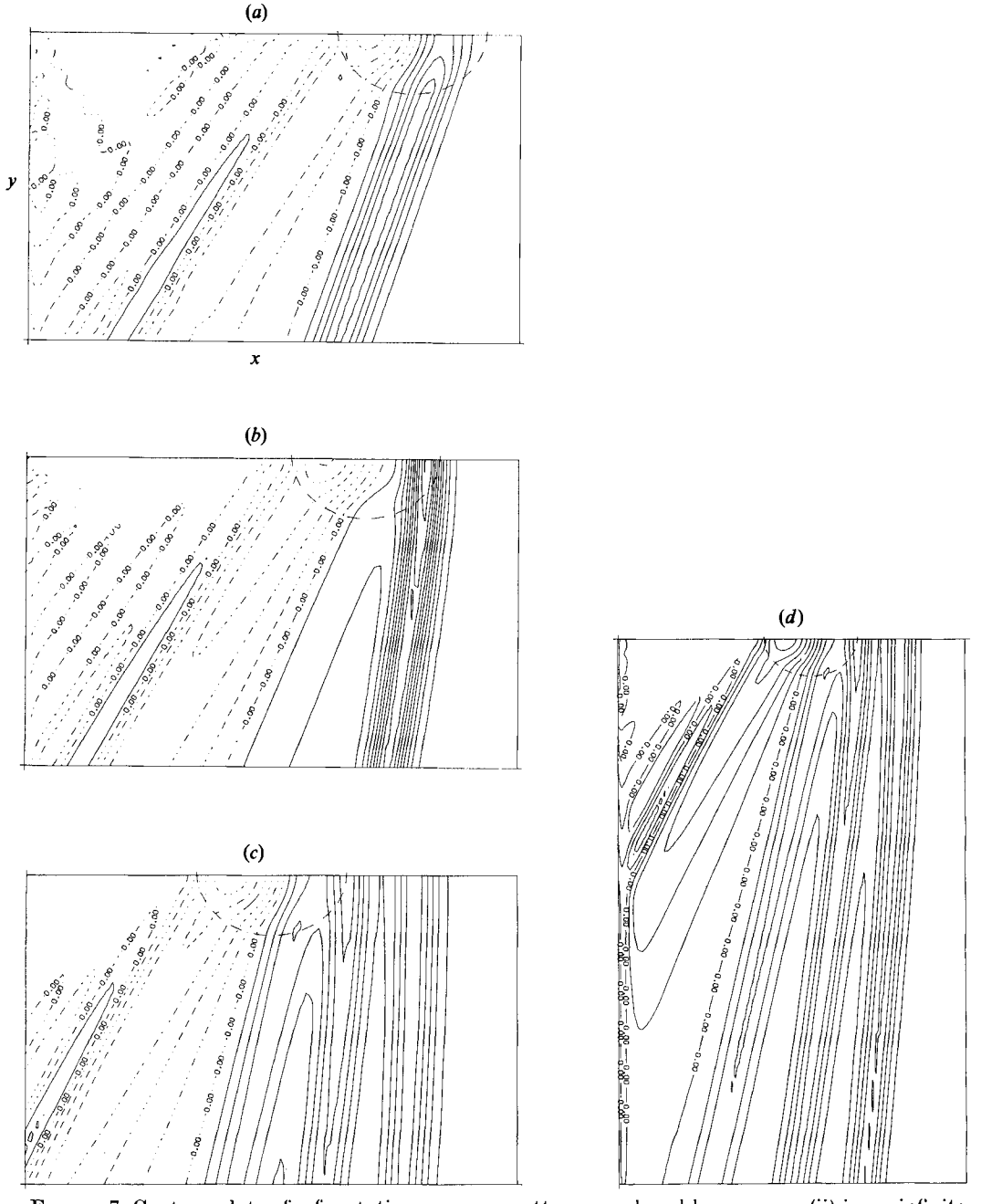

FIGURE 7. Contour plots of η for stationary wave patterns produced by pressure (ii) in an infinite fluid. The plots in (*a*)–(c) display only parts of the computational domains, and the contour interval is 0.02. (*a*) $F = 1.11$; (*b*) 1.09; (*c*) 1.05; (*d*) 1.05, the total computational window is depicted.

of the position of the free boundary has only a minor effect on the generated wave patterns, thereby indicating that this is not the case.

4.4. *A moving disturbance along a single wall*

A pressure field moving along a wall in semi-infinite sea will correspond to two separated fields moving in an infinite fluid. Therefore, one may assume that a

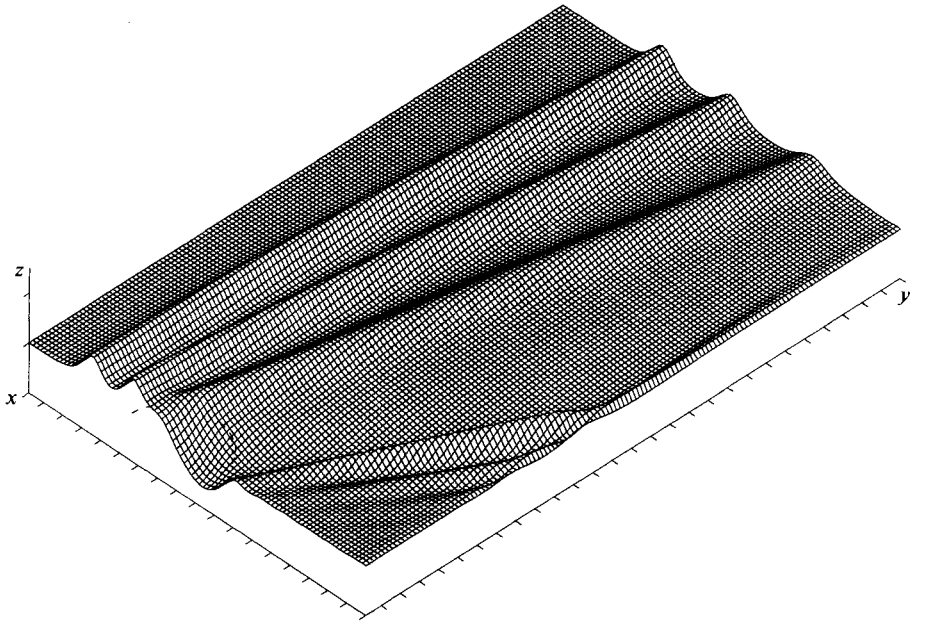

FIGURE 8. Perspective plot of the wave pattern generated by pressure (ii) in an unbounded fluid at $F = 1.05$ (the same as in figure 7*c*, *d*). The half-plane $y < 0$ is viewed from behind and across the x-axis.

stationary wave pattern is produced in this case as well. One principal difference from the previous cases is the presence of a lateral component of the wave resistance. It also turns out that the evolution of a steady state displays stronger and more persistent fluctuations than those observed for an unbounded fluid. The components of the wave resistance for the case $F = 1.05$, pressure (ii) and $y_0 = -40 = -4R$ are depicted in figure 10. While the longitudinal component displays moderate fluctuations from an average value of approximately -0.075 the lateral component, C_y, changes sign several times and reaches a maximum absolute value of about 0.005. Nevertheless, the integrated effect of C_y corresponds to a repulsion from the wall.

5. Conclusion

Upstream radiation of solitons has been predicted for channels as wide as 100 depths and blockage coefficients down to 0.006. A pressure field applied to the surface and a source distribution along a line represent two clearly different ways of modelling a ship. The fact that the two representations are generally found to produce very similar results demonstrates their applicability. In previous works several authors have stressed the significance of the blockage coefficient as the governing geometrical parameter. In the present calculations the blockage coefficient still determines the amplitude of the generated train of solitons but not its period or the limiting Froude number for which upstream radiation occurs. Upstream radiation in wide channels is closely related to the phenomenon of Mach reflection. The formation of two-dimensional crests and the transition between the radiative and the non-radiative regimes are appropriately analysed through the properties of Mach reflection. It also follows that we, at least theoretically, must expect upstream radiation to occur for channels of any width.

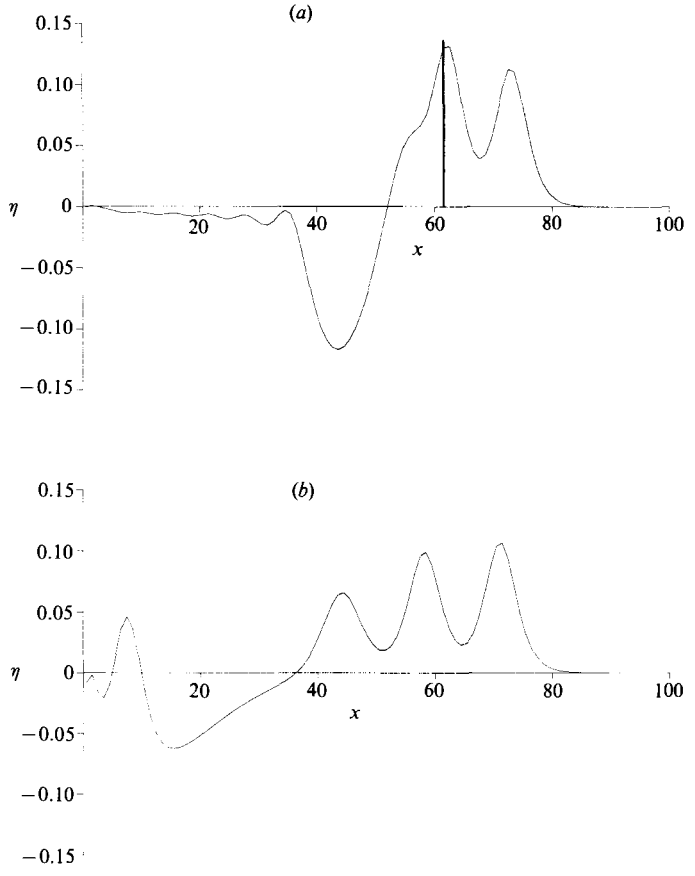

FIGURE 9. Cross-sections parallel to the x-axis of the wave pattern depicted in figures 7(c, d) and 8. (a) The surface elevation at $y = -0.5 = -\frac{1}{2}\Delta y$ that corresponds to the row of the grid being closest to the symmetry line. The front of the pressure field is marked by the solid vertical line at $x = 61.5$. We note that p does not exceed 20% of p_a until $x = 58$. (b) The surface elevation at $y = -49.5$.

	Pressure field			Source	
F	(i)	(ii)	(iii)	(i)	(ii)
1.000	—	$\geqslant 4$	—	—	—
1.025	—	3	2	$\geqslant 6$	$\geqslant 4$
1.050	$\geqslant 4$	2	1	$\geqslant 5$	2
1.075	3	1	0	$\geqslant 4$	1
1.100	2	1	—	—	—
1.125	—	0	—	—	—
1.150	1	—	—	—	—
1.175	0	—	—	—	—

TABLE 3. Number of upstream wave crests in a horizontally unbounded sea

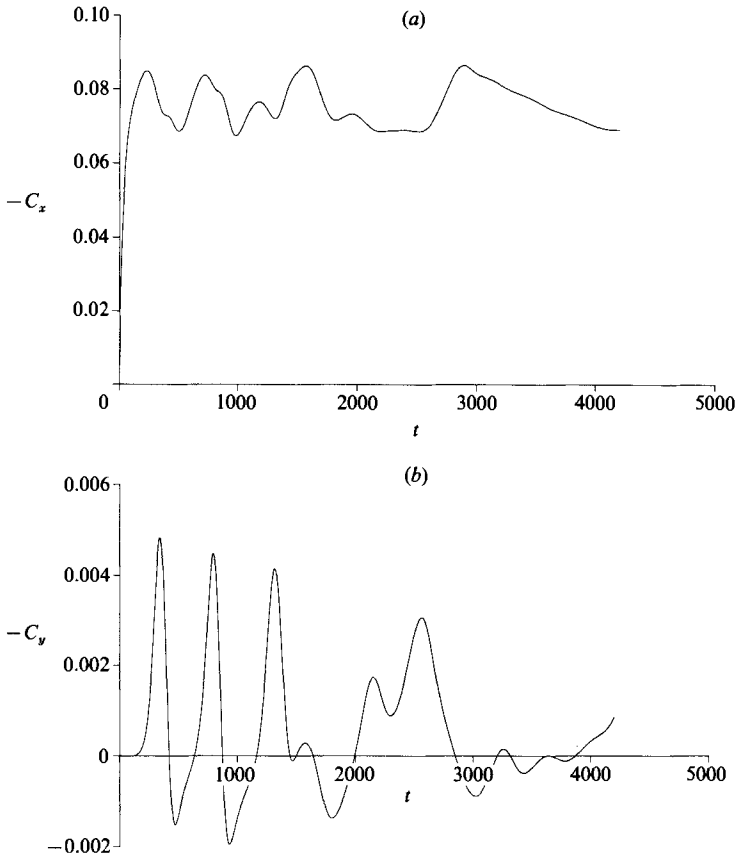

FIGURE 10. The components of the wave resistance, (*a*) C_x and (*b*) C_y, experienced by pressure field (ii) in a semi-infinite fluid. Additional parameters: $F = 1.05$, $y_0 = -40 = -4R$.

In infinite or semi-infinite fluid a periodic solution with upstream radiation of waves is impossible owing to lateral energy transport into the far field. From the present calculations we conclude that a stationary wave pattern always emerges. However, for Froude numbers slightly above 1 upstream influence is still experienced in the form of a finite number of soliton-like diverging waves situated ahead of the disturbance. In the neighbourhood of the symmetry line these crests interact to produce an upstream momentum and energy flux which counterbalances the lateral transport into the far field.

Appendix. Mach reflection

We consider a single soliton of height A reflecting from a wall at an angle of incidence ψ, which is defined as the angle between the direction of wave advance and the wall. For large ψ the incoming wave is subjected to normal reflection for which a reflected soliton identical to the incoming one with incidence $-\psi$ is produced. On the other hand, for ψ smaller than some $\psi_c(A)$ a different pattern of reflection, usually referred to as Mach reflection or abnormal reflection, evolves.

Mach reflection of solitons has been observed in experiments by Perroud (1957), Chen (1962), Sigurdsson & Wiegel (1962), Wiegel (1964) and Melville (1979). A

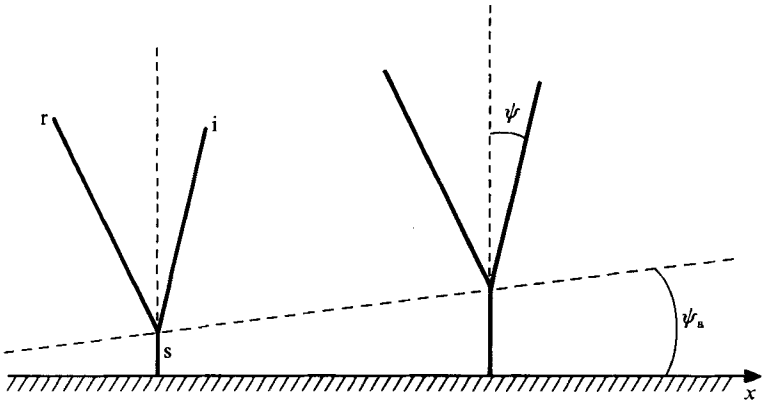

FIGURE 11. Definition sketch of the Mach reflection pattern: i, incoming wave crest; r, reflected wave crest, and s, Mach stem.

theoretical study of the phenomenon was carried out by Miles (1977*a*, *b*) who constructed an asymptotic solution ($t \to \infty$) for the fully developed wave pattern. The time evolution of abnormal reflection was later studied numerically by Funakoshi (1980). The phenomenon of Mach reflection is not confined to shallow-water solitons. On the contrary, as the name indicates, this type of reflection was first thoroughly discussed in gas dynamics, where it has been paid considerably more attention. A survey of this topic is given by Hornung (1986). Yue & Mei (1980) found theoretical evidence of Mach reflection in connection with diffraction of Stokes waves by a thin wedge. Abnormal reflection of Stokes waves must be expected to be important for formation of two-dimensional waves in the wake of a disturbance moving in a channel at slightly subcritical speed.

During Mach reflection of solitons a phase-locked triad of crests is created and no stationary wave pattern is reached. The apex of the incoming and reflected waves is moving away from the wall at a constant angle ψ_a and is connected to it by the third member of the triad; the Mach stem. The incidence of the reflected wave remains approximately equal to $-\psi_c$, for $\psi < \psi_c$ and its amplitude is less than A and tends to zero as $\psi \to 0$. A definition sketch of the wave pattern of Mach reflection is given in figure 11.

In the scaling introduced at the beginning of §4 some key results from Miles (1977) read

$$\psi_c = (3A)^{\frac{1}{2}}, \quad \psi_a = \tfrac{1}{3}(\psi_c - \psi). \tag{A 1}$$

The largest amplification at the wall is achieved for $\psi = \psi_c$ for which the Mach-stem height becomes $4A$. Determination of ψ_c by numerical integration in time is not a straightforward matter because the development of the Mach stem or the normal reflection pattern is extremely slow for ψ near ψ_c. The best approach seems to be to establish a linear relation between ψ_a and ψ and then take as ψ_c the ψ for which the extrapolated value of ψ_a becomes zero. Such a linear fit is usually excellent for values of ψ clearly below ψ_c, and tests involving long-time numerical simulations support the adequacy of this way of determining the critical angle of incidence. Melville (1979) used this technique to estimate ψ_c from his experimental data, but his wave tank was too short for the estimations to be appropriate. Because the amplifications at the wall are very large, different weakly nonlinear theories may give significantly different values for ψ_c. Thus, we cannot apply the values given by Miles in the

A	Present theory	Miles (1977*b*)	Funakoshi (1980)
0.10	26.9°±0.2	31.4°	—
0.05	20.3°±0.1	22.2°	20.8°

TABLE 4. Critical angle of incidence ψ_c for transition to Mach reflection

discussions of §4. Using the numerical methods described in §2, specifying the incoming wave according to (2.13)–(2.15) and treating the reflected wave by the radiation condition given in §4 we have calculated ψ_c for the Boussinesq equations (2.8) and (2.10). These values are listed in table 4 together with values obtained from (A 1) and a value extracted from the work of Funakoshi (1980) by the extrapolation procedure described above. The accuracy limits on ψ_c in the first column are obtained by grid refinement tests.

REFERENCES

CHEN, T. C. 1961 Experimental study on the solitary wave reflexion along a straight sloped wall at oblique angle of incidence. *U.S. Beach Erosion Board Tech. Memo.* no. 124.

ERTEKIN, R. C. 1984 Soliton generation by moving disturbances in shallow water: theory, computation and experiment. Ph.D. thesis, Department Naval Arch., Offshore Engng. University of California, Berkeley.

ERTEKIN, R. C., WEBSTER, W. C. & WEHAUSEN, J. V. 1984 Ship-generated solitons. In *Proc. 15th Symp. Naval Hydrodyn., Hamburg,* pp. 347–364. Washington, DC: National Academy of Sciences.

ERTEKIN,R. C., WEBSTER, W. C. & WEHAUSEN, J. V. 1986 Waves caused by a moving disturbance in a shallow channel of finite width. *J. Fluid Mech.* **169**, 275–292.

FUNAKOSHI, M. 1980 Reflection of obliquely incident solitary waves. *J. Phys. Soc. Japan* **49**, 2371–2379.

GRAFF, W. 1962 Untersuchungen über die Ausbildung des Wellenwiderstandes im Bereich der Stauwellengeschwindigkeit in flachem, seitlich beschränktem Farhwasser. *Schifftechnik* **9**, 110–122.

HORNUNG, H. 1986 Regular and Mach reflection of shock waves. *Ann. Rev. Fluid Mech.* **18**, 33–58.

HUANG, D. B., SIBUL, O. J., WEBSTER, W. C., WEHAUSEN, J. V., WU, D. M. & WU, T. Y. 1982 Ships moving in the transcritical range. In *Proc. Conference on Behaviour of Ships in Restricted Waters, Varna, Bulgaria,* vol. 2, pp. 26.1–26.9.

KARPMAN, V. I. 1967 The structure of two-dimensional flow around bodies in dispersive media. *Sov. Phys., J. Exp. Theor. Phys.* **23**, 1102–1111.

KATSIS, C. & AKYLAS, T. R. 1987 On the excitation of long nonlinear water waves by a moving pressure distribution. Part 2. Three-dimensional effects. *J. Fluid Mech.* **177**, 49–65.

MEI, C. C. 1976 Flow around a thin body moving in shallow water. *J. Fluid Mech.* **77**, 737–751.

MEI, C. C. 1986 Radiation of solitons by slender bodies in a shallow channel. *J. Fluid Mech.* **162**, 53–67.

MELVILLE, W. K. 1979 On the Mach reflection of a solitary wave. *J. Fluid Mech.* **98**, 285–297.

MILES, J. W. 1977*a* Obliquely interacting solitary waves. *J. Fluid Mech.* **79**, 157–169.

MILES, J. W. 1977*b* Resonantly interacting solitary waves. *J. Fluid Mech.* **79**, 171–179.

PEDERSEN, G. & RYGG, O. B. 1987 Numerical solution of the three dimensional Boussinesq equations for dispersive surface waves. *University of Oslo, Research Rep. in Mechanics* **1**.

PERROUD, P. H. 1957 The solitary wave reflection along a straight vertical wall at oblique incidence. Ph.D. thesis. University of California, Berkeley.

SCHMIDT-STIEBITZ, H. 1966 Die Abhängigkeit des Schiffswiderstandes von flachwasserbedingten Umströmungs- und Wasserspiegelveränderungen. *Schiff und Hofen* **18**, 381–395.

SIGURDSSON, G. & WIEGEL, R. L. 1962 Solitary wave behavior at concave barriers, Calcutta. *The Port Engineer*, **9**, 4, 4–8.

THEWS, J. G. & LANDWEBER, L. 1935 The influence of shallow water on the resistance of a cruiser model. *US Experimental Model Basin, Navy Yard, Washington, D.C., Rep.* 414.

WIEGEL, R. L. 1964 *Oceanographical Engineering*. Prentice-Hall.

WU, D. M. & WU, T. Y. 1982 Three-dimensional nonlinear long waves due to moving surface pressure. In *Proc. 14th Symp. Naval hydrodyn.*, pp. 103–129. Washington, DC: National Academy of Sciences.

YUE, D. K. P. & MEI, C. C. 1980 Forward diffraction of Stokes waves by a thin wedge. *J. Fluid Mech.* **99**, 33–52.